Article

Global Gust Climate Evaluation and Its Influence on Wind Turbines

Christopher Jung *, Dirk Schindler, Alexander Buchholz and Jessica Laible

Environmental Meteorology, University of Freiburg, 79085 Freiburg, Germany;
dirk.schindler@meteo.uni-freiburg.de (D.S.); alex.buchholz@ymail.com (A.B.); jessica.laible@web.de (J.L.)
* Correspondence: christopher.jung@mail.unr.uni-freiburg.de; Tel.: +49-761-203-6822

Abstract: Strong gusts negatively affect wind turbines in many ways. They (1) harm their structural safety; (2) reduce their wind energy output; and (3) lead to a shorter wind turbine rotor blade fatigue life. Therefore, the goal of this study was to provide a global assessment of the gust climate, considering its influence on wind turbines. The gust characteristics analyzed were: (1) the gust speed return values for 30, 50 and 100 years; (2) the share of gust speed exceedances of cut-out speed; and (3) the gust factor. In order to consider the seasonal variation of gust speed, gust characteristics were evaluated on a monthly basis. The global monthly wind power density was simulated and geographical restrictions were applied to highlight gust characteristics in areas that are generally suitable for wind turbine installation. Gust characteristics were computed based on ERA-interim data on a $1° \times 1°$ spatial resolution grid. After comprehensive goodness-of-fit evaluation of 12 theoretical distributions, Wakeby distribution was used to compute gust speed return values. Finally, the gust characteristics were integrated into the newly developed wind turbine gust index. It was found that the Northeastern United States and Southeast Canada, Newfoundland, the southern tip of South America, and Northwestern Europe are most negatively affected by the impacts of gusts. In regions where trade winds dominate, such as eastern Brazil, the Sahara, southern parts of Somalia, and southeastern parts of the Arabian Peninsula, the gust climate is well suitable for wind turbine installation.

Keywords: gust speed; gust factor; return values; cut-out speed; Wakeby distribution; wind turbine gust index

1. Introduction

Constant electricity supply is essential for both production and consumption of goods and services [1]. Extreme weather conditions can have serious negative impacts on the electricity supply. Windstorms and tropical storms are amongst the most harmful disturbances for the electricity grid [2]. Minor storm-related power outages are mainly caused by damage from trees falling on local electricity distribution lines and poles, while major outages are often the result of damage to electricity transmission lines [3,4]. In the USA alone, it is estimated that storm-related outages cost between $20 billion and $55 billion annually [3].

The utilization of wind energy poses new challenges to storm risk management in the energy industry. Wind turbines are used to convert the kinetic energy of airflow first into mechanical and then into useful electric energy [5]. In order to maximize power output, wind turbines are generally built in areas where average wind speed (x) is high. However, during storm events, x can reach a destructive level. The short-time (~3 s) fluctuations of x, which are called gusts [6], are a critical issue to the infrastructure and environment [7].

There are several ways gust characteristics (GC) influence wind turbines. First and foremost, extreme gust speed (GS) poses a great risk to the structural safety of wind turbines [8]. The survival

speed indicates until which *GS* a wind turbine stays unharmed. Typical survival speed values are in the range between $GS = 50$ m s^{-1} and $GS = 70$ m s^{-1} [9]. The wind turbine design is typically developed based on the 50-year return value of *GS* to consider the most severe storm events [10].

In order to prevent damage, wind turbines are shut down at cut-out speed [11], although *x* and wind power density (*WPD*) are high. A typical cut-out speed of many wind turbines is 25.0 m·s^{-1}. Frequent shut-downs can lead to energy yield losses.

Strong vertical wind shear and gustiness negatively influence the technical integrity of wind turbines. For instance, gustiness reduces the rotor blade fatigue life [12]. Gustiness of the airflow is typically expressed by the gust factor (*GF*). *GF* is defined as the ratio between *GS* and *x* [13].

The following example emphasizes the importance of *GC* for the wind energy sector: In 2005, winter storm Gudrun passed over Ireland, Great Britain, Denmark, Norway, and Sweden. On the coast of Denmark, gust speed reached values up to 46 m s^{-1} in 10 m above ground level (a.g.l.). At that time, 5400 wind turbines operated in Denmark. There was great danger that the survival speed of the wind turbines could be surpassed by the storm-related gusts and a great number of the wind turbines would be damaged by the storm. In order to prevent damage, most wind turbines were shut down after *GS* exceeded cut-out speed. This led to a sharp decrease in the produced amount of wind energy locally, to less than 5%. The abruptly missing wind energy had to be substituted by energy imports from neighboring countries [14].

Despite its importance, little research involving *GC* has been carried out [8]. Often theoretical distributions are used to describe the long-term gust climate. In several studies the two-parameter Gumbel distribution (Gu) was applied to capture extreme *x* characteristics [15–18]. The three-parameter Generalized Extreme Value distribution (GEV) and Gu were used for extreme *x* value estimation in China [8]. Morgan et al. Reference [10] evaluated the capability of numerous theoretical distributions to capture the extreme tails of *x* values in North American offshore areas and found that the two-parameter Lognormal distribution (L) is suitable. The two-parameter Weibull distribution (Wei) was applied by [19] and the three-parameter inverse Burr distribution by [20] to evaluate extreme *x* values.

The abovementioned studies mainly focused on *GC* on a regional level. However, as electricity consumption is covered increasingly by wind energy in many countries, it is of great interest and importance to evaluate where, when, and how frequently *GS* values dangerous for regular, continuous wind turbine operation occur. Thus, a detailed description of the global gust climate is an essential precondition for a comprehensive assessment of gust-related hazards to wind turbine operation, especially in the light of large-scale storm events. The diversity of the conceptual frameworks, samples and results reported from previous studies does not allow for such a general and global description of *GC*.

Thus, the goal of this investigation is to systematically analyze the (1) long-term return values of *GS*, (2) occurrences of *GS* exceeding the wind turbine cut-out speed, and (3) *GF* on a global scale. For a global overview of the influence of gusts on wind turbines, these *GC* are integrated into the newly developed wind turbine gust index (*WTGI*).

2. Material and Methods

2.1. Overview

In order to evaluate *GC* and to determine *WTGI* the following steps were carried out: (1) obtaining global grid point related *GS* and *x* time series in the period from 1 January 1979 to 31 December 2015; (2) monthly segmentation of *GS* and *x* time series; (3) distribution fitting and goodness-of-fit (GoF) evaluation of annual maximum of *GS* empirical probability density functions (epdf); (4) computation of *GS* return values for 30 y (GS_{30yr}), 50 y (GS_{50yr}) and 100 y (GS_{100yr}); (5) determination of the monthly cut-out speed exceedances of *GS* (*SOC*); (6) calculation of *GF* using *GS* as well as *x*; and (7) integration of GS_{50yr}, *SOC* and *GF* into *WTGI* by normalization.

Distribution fitting of *GS* was necessary to extrapolate *GS* values to return levels exceeding the period of available data. The goodness-of-fit of evaluation of various theoretical distributions was carried out in order to determine the most appropriate distribution for calculating the gust speed return values.

2.2. Data

Maximum *GS* obtainable for a height of 10 m a.g.l. was provided from the ECMWF ERA-Interim reanalysis project [21]. ECMWF ERA-Interim reanalysis gust speed is only available for 10 m a.g.l., which is the standard measuring height for gust speed according to the World Meteorological Organization [22]. The current data base and measurement process of gust speed prevents a globally consistent gust climate evaluation in wind turbine hub height. Thus, an assessment of the global gust climate can best be achieved by using ECMWF ERA-Interim data in 10 m a.g.l. According to the power law [23], gust speed increases with increasing height a.g.l. based on thermally and mechanically induced mixing, wind speed, air temperature conditions, elevation, time of day, season, and the nature of the terrain [12]. Deacon [24] showed that the increase of gust speed with height to be markedly less than the increase of average wind speed. Therefore, gust analysis at 10 m a.g.l. could assess its impact on wind turbines installed at much higher heights.

The reanalysis data cover the entire surface of the earth with grid cells at a spatial resolution of $1° \times 1°$. The maximum *GS* values in a three hour period are available for 00 coordinated universal time (UTC), 03 UTC, 06 UTC, 09 UTC, 12 UTC, 15 UTC, 18 UTC and 21 UTC covering the period from 1 January 1979 to 31 December 2015.

Furthermore, the zonal (*u*) and meridional (*v*) wind vector components at 00 UTC, 06 UTC, 12 UTC, and 18 UTC in the same period at 10 m a.g.l. were used. The wind vector components were applied to compute average wind speed:

$$x = \sqrt{u^2 + v^2}. \tag{1}$$

It is well known that wind speed characteristics vary throughout the year [25,26], therefore both *GS* and *x* time series were separated by month.

2.3. Distribution Fitting

The *GS* return values were estimated by the block maxima method using the Matlab version 2017a software (The MathWorks Inc., Natick, MA, USA). This approach is based on the idea that the highest *GS* values of time-limited blocks (often years) from a parent distribution can be used to estimate *GS* return values by fitting them to an extreme value distribution [27,28]. The block maxima method was applied by first obtaining the annual maximum *GS* values for each month. Subsequently, the annual maximum *GS* time series were transformed into epdfs and empirical cumulative distribution functions (ecdfs). Afterwards, twelve different theoretical distributions were fitted to monthly *GS* epdfs and ecdfs (Table 1). The number of distribution's parameters (*NP*) range from two to five. The parameter estimation methods (PEM) L-moment method (LM), Maximum Likelihood estimation (ML) and Moment method (M) were used to find the parameters of each *GS* epdf [29].

Table 1. Tested distributions with their abbreviation (S), number of parameters (*NP*), and parameter estimation methods (PEM).

Distribution	S	*NP*	PEM
Gamma	G	2	ML, LM
Gumbel	Gu	2	ML, LM
Lognormal	L	2	ML, M
Weibull	Wei	2	ML, M, LM
Gen. Extreme Value	GEV	3	ML, LM
Generalized Logistic	GL	3	LM

Table 1. *Cont.*

Distribution	S	*NP*	PEM
Gen. Normal	GN	3	LM
Gen. Pareto	GP	3	LM
Pearson 3	P3	3	LM
Lognormal	L3	3	LM
Kappa	K	4	LM
Wakeby	Wak	5	LM

2.4. Goodness-of-Fit Evaluation

In order to select the most suitable of the theoretical distributions to fit *GS* epdfs, two GoF metrics were applied. The first GoF metric was the Kolmogorov–Smirnov (*KS*) statistic [30]. *KS* is defined as the maximum absolute difference between ecdf and the cumulative distribution function of the theoretical distribution (cdf):

$$KS = max \left| F_i - \hat{F}_i \right| \tag{2}$$

where F_i is the *i*th ecdf value and $\hat{F}_i$ is the estimated cdf of the *i*th ecdf value.

The second GoF metric was the Anderson–Darling (*AD*) statistic [31]:

$$AD = -n - \frac{1}{n} \sum_{i=1}^{n} (2i - 1)\{ \ln F[\text{GS}_i] + \ln[1 - F(\text{GS}_{n-i+1})] \} \tag{3}$$

where *n* is the sample size. The lower the *KS* and *AD* values, the better the GoF of the theoretical distribution.

2.5. Wakeby Distribution

According to GoF evaluation, Wak is the most appropriate theoretical distribution to characterize *GS* epdfs. It is defined by one location parameter (ε), two scale parameters (α, γ), and two shape parameters (β, δ). The probability density function (pdf) of Wak is [32]:

$$f_{WAK}(GS; \alpha, \beta, \gamma, \delta, \varepsilon) = \left\{ \alpha[1 - F(GS)]^{\beta-1} + \gamma[1 - F(GS)]^{-\delta-1} \right\}^{-1} \tag{4}$$

Most often, Wak is presented by its quantile function [33,34]:

$$F_{WAK}^{-1}(GS; \alpha, \beta, \gamma, \delta, \varepsilon) = \varepsilon + \frac{\alpha}{\beta}[1 - (1 - F)^{\beta}] - \frac{\gamma}{\delta}[1 - (1 - F)^{-\delta}] \tag{5}$$

The cdf of Wak can be computed by numerically inverting F_{WAK}^{-1} [35]. The parameters of Wak were estimated by LM [36] for every month and grid cell.

2.6. Determination of Gust Characteristics

By applying Wak, *GS* return values were estimated. The cumulative probabilities related to return periods (*T*) of 30, 50 or 100 yr were computed by [37]:

$$F(GS) = 1 - \left(\frac{1}{T} \right) \tag{6}$$

Afterwards, it was possible to estimate *GS* return values by Equation (5) for each grid-cell, month, and *T*. *SOC* was determined by counting the grid point-related, monthly cut-out speed (25 m s^{-1}) exceedances of *GS* in the investigation period. *GF* was computed by dividing the maximum *GS* in a six-hour period by *x* related to the same period. Afterwards, the median of the monthly, six hourly *GF* values was computed ($\widetilde{GF}$).

2.7. Calculation of Wind Turbine Gust Index

The wind turbine gust index was developed to enable a global comparison of the threat gusts pose to the wind turbine utilization in different regions of the world. For *WTGI* calculation, the monthly gust characteristics GS_{50yr}, $(\widetilde{GF})$ and *SOC* were normalized according to [38]:

$$GC'_i = \frac{GC_i - GC_i^{min}}{GC_i^{max} - GC_i^{min}} \tag{7}$$

with GC'_i being the normalized statistic and GC_i^{min} and GC_i^{max} are the minimum and maximum original values for the statistic, respectively. Furthermore, all monthly GC'_i were added up, yielding *WTGI*. The grid point-related *WTGI* values were classified into eight classes by quantiles. Thus, class 1 indicates that a location belongs to the 12.5% of geographically accessible area with the least impact of gusts. Accordingly, class 8 indicates that a location belongs to the 12.5% of geographically accessible area with the greatest impact of gusts. The classification was carried out separately for geographically accessible onshore and offshore areas.

2.8. Determination of the Meteorological and Geographical Wind Energy Potential

The meteorological and geographical wind energy potential was evaluated in order to highlight *WTGI* in areas, which are generally suitable for wind turbine installation.

WPD was used to assess the meteorological wind energy potential, according to:

$$WPD = \frac{1}{2}\rho x^3 \tag{8}$$

where ρ is the air density, which was calculated by:

$$\rho = \frac{APR}{R \cdot TA} \tag{9}$$

with *APR* being the atmospheric pressure, *TA* the air temperature, and *R* the atmospheric gas constant ($287.058 \text{ J kg}^{-1} \text{ K}^{-1}$). *APR* and *TA* were obtained from ERA-Interim data for the same period as *x*.

Ice-covered regions, lakes, urban areas, wetlands, evergreen forests [39], conservation areas [40], sloped areas (>10°) [41,42], and permafrost areas [43,44] were excluded using ESRI's ArcGIS 10.2, since onshore wind turbine installation is not (or only to a limited extent) possible in such regions.

Offshore areas unsuitable for wind turbine installation were defined as areas where the sea depth exceeds 200 m [45].

3. Results and Discussion

3.1. Goodness-of-Fit Evaluation of Gust Speed Distributions

Results of GoF evaluation indicate that Wak-LM is the overall most appropriate theoretical distribution to reproduce *GS* epdfs. According to *KS*, Wak-LM fits 42–44% of all evaluated monthly *GS* epdfs best (Table 2). For two thirds of all *GS* epdfs, Wak-LM ranked between one and three. No clear GoF differences between onshore and offshore *GS* epdfs or between *GS* epdfs related to different months occurred. Thus, it can be assumed that the high fitting accuracy of Wak-LM is not limited to any specific region or month. Therefore, Wak-LM was used to compute monthly *GS* return values. GEV-LM fits 4–5% of all monthly *GS* epdfs best and ranked between one and three at ~25% of all grid cells. Other distributions that fit a remarkable number of GS epdfs very well were GL-LM and K-LM. It is striking that PEM of the first eight distributions that ranked most often between one and three was LM. Thus, it can be concluded that LM is the most appropriate PEM for a small sample size. Whereas Wei fitted by LM is at 21–22% of the grid cells among the top three distributions, Wei fitted by M and ML ranked only 1–2% among the three most appropriate distributions.

Table 2. Results from goodness-of-fit comparison of the theoretical distributions. The table shows the share of distribution (%) ranked one to three (first number)/best (second number) at all evaluated grid cells according to the comparison of the monthly Kolmogorov–Smirnov (*KS*) statistic.

S	Jan	Feb	Mar	Apr	May	Jun	Jul	Aug	Sep	Oct	Nov	Dec
Wak-LM	66/42	66/42	66/43	67/43	67/44	66/43	67/44	67/44	66/43	66/43	67/44	67/43
GL-LM	30/11	32/11	33/11	32/11	33/12	31/11	34/12	33/11	33/11	32/12	34/12	34/11
K-LM	29/9	28/9	28/9	28/9	27/8	29/9	27/9	27/9	27/8	28/9	27/9	28/9
GEV-LM	24/4	24/4	26/5	25/4	24/4	25/5	24/4	25/4	24/4	25/4	26/4	25/4
Wei-LM	22/6	21/6	21/6	22/6	21/6	22/6	21/6	21/6	22/6	21/6	21/6	21/6
GN-LM	14/1	17/2	17/2	17/2	17/2	18/2	18/2	17/2	18/2	17/2	17/2	17/2
GP-LM	15/5	13/4	13/4	14/4	13/4	14/4	13/4	13/4	13/4	13/4	12/4	13/4
L3-LM	15/2	13/1	13/1	12/1	13/1	13/1	13/1	13/1	13/1	13/1	12/1	12/1
L-ML	12/2	12/2	11/2	13/2	12/2	12/2	12/2	12/2	12/2	13/2	12/2	12/2
GEV-ML	12/3	12/3	12/3	11/3	12/3	11/3	12/3	12/3	12/3	12/3	12/3	12/3
Gu-ML	12/4	11/3	11/3	11/3	11/3	10/3	10/3	11/3	11/3	10/3	11/3	11/3
P3-LM	10/2	11/2	11/2	10/2	10/2	10/2	10/2	10/2	11/3	10/2	10/2	10/2
L-M	10/2	10/3	9/2	10/2	10/2	10/2	10/2	10/2	10/2	10/2	10/2	10/2
G-LM	9/2	9/2	9/2	10/2	10/2	9/2	9/2	9/2	9/2	10/2	10/2	9/2
Gu-LM	10/2	10/3	10/2	9/2	9/2	8/2	9/2	9/2	9/2	8/2	9/2	9/2
G-ML	7/1	7/1	6/1	7/1	7/1	7/1	7/1	7/1	7/1	7/1	8/1	7/1
Wei-M	2/0	2/0	1/0	2/0	2/0	2/0	2/0	2/0	2/0	2/1	2/0	2/0
Wei-ML	2/0	2/0	1/0	1/0	2/0	2/0	2/0	2/0	2/0	1/0	2/0	2/0

GoF results obtained for *AD* are quite similar to *KS* (Table 3). For more than 60% of all grid cell-related *GS* epdfs, Wak-LM is among the three top ranked distributions, regardless of month. It provides the highest fitting accuracy for ~50% of all grid cell related epdfs. In contrast to *KS*, *AD* is more sensitive to the epdfs tails. Thus, it can be concluded that Wak-LM is suitable for reproducing both the central parts and the upper tails of the evaluated epdfs. The percentage share of GEV-LM ranking between one and three is in all months at least 33%, which is clearly higher than for *KS*. One reason might be that GEV-LM reproduces the upper tails of the evaluated epdfs very well. It is noticeable that K-LM is the only distribution, beside Wak-LM, that provides the best GoF according to *AD* for more than 10% of all grid cell related *GS* epdfs in all months. Other theoretical distributions that provide reasonable fits to *GS* epdfs are GL-LM, GN-LM and Wei-LM, which rank between one and three for more than 30% at all grid-cell related epdfs in most months. On the other hand, the share of GP-LM, G-ML, L-M, Wei-ML, and Wei-M ranking between one and three is below 3% in all months, indicating that these combinations of theoretical distribution and PEM should not be used for estimating *GS* return values.

Table 3. Results from goodness-of-fit comparison of the theoretical distributions. The table shows the share of distribution (%) ranked one to three (first number)/best (second number) at all evaluated grid cells according to the comparison of the monthly Anderson–Darling (*AD*) statistic.

S	Jan	Feb	Mar	Apr	May	Jun	Jul	Aug	Sep	Oct	Nov	Dec
Wak-LM	61/49	62/50	62/50	62/38	64/52	62/50	62/51	62/50	62/51	63/50	62/51	63/50
GL-LM	38/12	40/12	42/13	39/7	40/12	39/12	42/13	42/13	41/13	40/13	43/14	42/13
GEV-LM	34/6	36/6	35/6	33/5	34/5	36/6	34/6	35/6	36/6	34/5	34/5	35/5
K-LM	32/13	31/14	31/13	55/37	30/13	32/14	30/13	30/13	29/12	31/13	30/12	31/13
Wei-LM	32/8	30/8	29/7	31/8	31/8	33/8	31/8	30/8	30/7	31/8	30/7	30/8
GN-LM	33/3	31/3	30/3	23/1	31/3	31/3	32/3	30/3	31/3	31/3	31/3	30/3
L3-LM	19/2	20/2	21/2	16/1	20/2	20/2	20/2	21/2	20/2	21/2	20/2	20/2
P3-LM	18/3	17/2	16/3	15/2	16/2	16/2	16/2	16/2	16/2	17/3	15/2	16/2
GEV-ML	10/1	10/1	11/1	7/0	9/1	9/1	9/1	10/1	10/1	9/1	10/1	11/1
Gu-ML	5/1	4/1	5/1	4/1	4/1	4/1	4/1	5/1	4/1	4/1	4/1	5/1
Gu-LM	4/0	4/0	5/0	4/0	4/0	4/0	4/0	5/0	5/0	4/0	4/0	4/0
L-ML	4/0	4/0	4/0	4/0	4/0	4/0	4/0	4/0	2/0	4/0	4/0	4/0
G-LM	3/0	3/0	3/0	3/0	4/0	3/0	3/0	3/0	3/0	3/0	3/0	3/0
G-ML	2/0	2/0	2/0	2/0	4/0	2/0	2/0	2/0	2/0	2/0	2/0	2/0
L-M	2/0	2/0	2/0	1/0	4/0	2/0	2/0	2/0	2/0	2/0	2/0	2/0
GP-LM	2/1	2/1	2/0	2/1	2/1	2/1	2/1	2/1	2/1	2/1	2/1	2/1
Wei-ML	1/0	1/0	1/0	1/0	1/0	1/0	1/0	1/0	1/0	1/0	1/0	1/0
Wei-M	1/0	1/0	0/0	0/0	0/0	0/0	0/0	0/0	0/0	0/0	1/0	1/0

3.2. Gust Characteristics around the World

The spatial distribution of GS_{30yr} is characterized by remarkable differences between ocean and land surfaces (Figure 1a). Highest GS_{30yr} values (>40 m s^{-1}) were simulated over the Atlantic Ocean and Pacific Ocean between 40° N to 70° N. At the equator, GS_{30yr} values are clearly lower (<20 m s^{-1}). Near the coasts, GS_{30yr} values are generally lower than on the high seas. Onshore areas where high GS_{30yr} values occur are in the Midwestern United States, Northwestern Europe, and the southern tip of South America. In these regions, GS_{30yr} values exceed 30 m s^{-1} on large areas. This is a result of the west wind drift in the northern hemisphere, which is connected with high GS_{30yr} values. In contrast, GS_{30yr} values in many countries belonging to the lower latitudes are low. In South American countries such as Peru, Colombia, Brazil, as well as in African countries such as Congo, DRC, or Ethiopia, GS_{30yr} values are often below 15 m s^{-1}. Despite the fact that high x values occur in the trade wind belt, the GS_{30yr} values are lower than in many other areas. Therefore, in nearly all parts of Africa GS_{30yr} values are below 30 m s^{-1}.
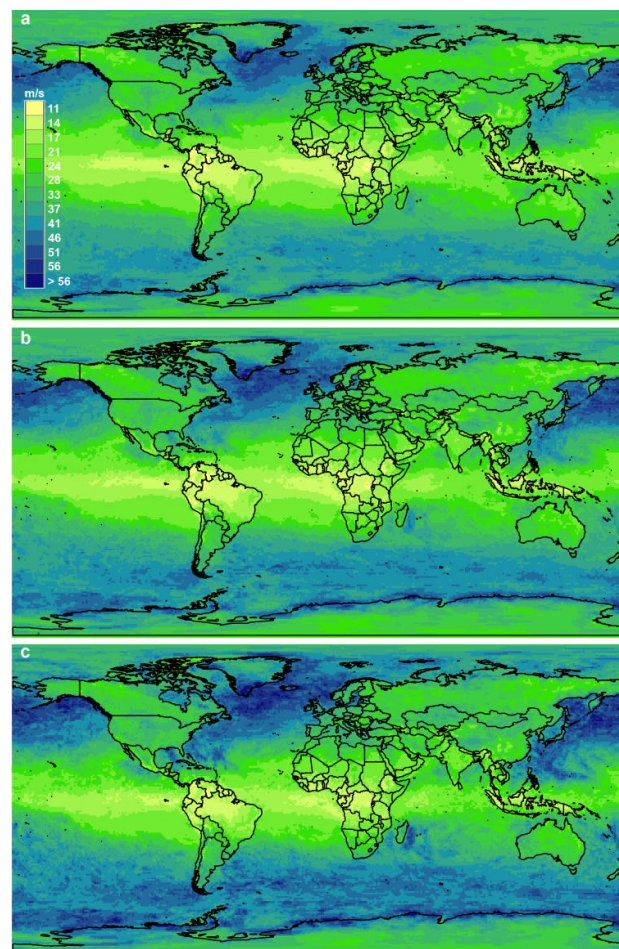
Figure 1. Gust speed (*GS*) values for a return period of (**a**) 30 years (GS_{30yr}); (**b**) 50 years (GS_{50yr}); and (**c**) 100 years (GS_{100yr}).

The global distribution of GS_{50yr} is displayed in Figure 1b. The main characteristics of GS_{50yr} patterns are similar to GS_{30yr}. In areas where tropical storms occur, GS_{50yr} values are higher than in the surrounding areas. For instance, in the Gulf of Mexico, the influence of strong hurricanes leads to GS_{50yr} values up to 40 m s^{-1}. Near Madagascar's coast, tropical storm-related GS_{50yr} values exceed 40 m s^{-1}. In Japan, typhoons can cause tremendous damage to the infrastructure. At many offshore grid cells near the Japanese coast, GS_{50yr} values are close to 50 m s^{-1}. Planning of offshore

wind turbine projects in these areas must consider the strong wind loads related to tropical storms. Small-scale severe weather events like tornadoes are less likely to be covered in the produced maps, due to the spatial resolution. In the "Tornado Alley" in the Midwestern United States GS_{50yr} values exceed 30 m s^{-1}. However, it must be recognized that *GS* values related to strong tornadoes clearly surpass such values. High GS_{50yr} values in Europe are not caused by tropical storms, but by large-scale windstorms. In large parts of Western Europe, especially in Ireland, Great Britain, France, the Benelux countries, and Germany, GS_{50yr} values are ~30 m s^{-1}.

The windstorm-related GS_{100yr} values near the French Atlantic coast are nearly 40 m s^{-1} (Figure 1c). On the Scottish Western Isles, GS_{100yr} values are up to 56 m s^{-1}. Similar high GS_{100yr} values were simulated on the west coast of Iceland. Some areas in the Mediterranean Sea, such as the southwest of the Crete Island and the south of Croatia, are exposed to $GS_{100yr} > 35$ m s^{-1}. Both Canadian coasts are influenced by very high GS_{100yr} values. On the west coast, some grid cell-related GS_{100yr} values are close to 60 m s^{-1}. The GS_{100yr} values on the east coast are slightly lower, but clearly exceed 40 m s^{-1}. Overall, at 29% of all onshore grid cells, GS_{100yr} exceeds 30 m s^{-1}. GS_{100yr} values higher than 40 m s^{-1} were simulated at 6.0% and $GS_{100yr} > 50$ m s^{-1} occurs at 1.2% of all onshore grid cells.

Frequently recurring periods of *GS* exceeding cut-out speed can lead to energy yield loss. Such conditions occur over the ocean areas of the mid-latitudes where *SOC* often exceeds 2.5% (Figure 2). Onshore areas are clearly less affected by *SOC* > 2.5%. They are limited to some regions near the coast of Chile, western Ireland and Great Britain, Canada, Alaska, Greenland, and Iceland. On the Changtang plateau in China, *SOC* exceeds 0.25% in vast areas. In large parts of mid-latitude countries like Canada, USA, Argentina, Japan, and the western European countries, *SOC* values exceed 0.01%. As can be clearly seen, very low *SOC* values dominate in the low latitudes and near the equator. In northern parts of South America, Africa, India, and Southeast Asia, almost no periods where $GS > 25$ m s^{-1} occur. Exceptions are where tropical cyclones are frequent such as the Gulf of Mexico, near Madagascar, and the Bay of Bengal. Overall, at 27.8% of all grid cells *SOC* = 0. On the other hand, *GS* exceeds 25 m s^{-1} during 2.5% of all periods at 8.1% of all grid cells.
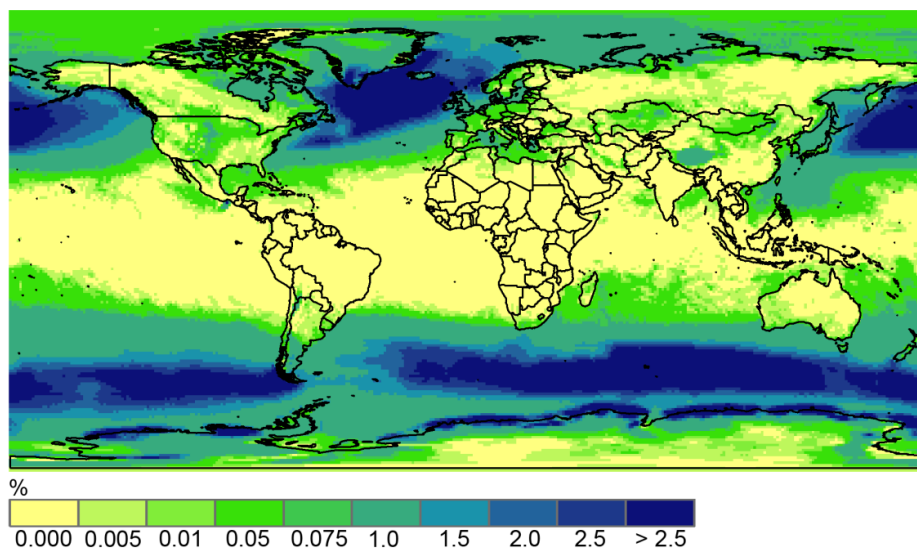

Figure 2. Share of three-hour periods when gust speed (*GS*) exceeds 25.0 m s^{-1} (*SOC*) in the investigation period.

Surface roughness disturbs the laminar air flow. Consequently, air flow over rough surfaces becomes more turbulent and gust factors increase [46]. Therefore, high $\widetilde{GF}$ values can be found where surface roughness is high (Figure 3). In areas where tropical forests dominate, $\widetilde{GF}$ is often > 3.0. Beside tropical forests, large mountain ranges cause high surface roughness, and consequently high $\widetilde{GF}$

values. Such conditions can be found in the Rocky Mountains, the Alps and the Himalaya, where $\widetilde{GF}$ values related to tropical forests are even exceeded ($\widetilde{GF} > 4.0$). In Japanese onshore areas, $\widetilde{GF}$ values lie between 2.5 and 3.0. Lowest $\widetilde{GF}$ can be found over ocean areas, Greenland and the Antarctica ($\widetilde{GF} \sim 1.4$). Over European land areas, $\widetilde{GF}$ is often ~ 2.0. In the Midwestern of the United States, the Sahara and Kazakhstan, low $\widetilde{GF}$ values were simulated, indicating that the negative influence of gusts on the technical integrity is small. Overall, at 35.9% of all grid cells $\widetilde{GF}$ is below 1.4. At 84.8% of all grid cells, $\widetilde{GF}$ does not exceed 2.0. Very high $\widetilde{GF}$ values (>3.0) can be found on 2.5% of the earth's surface.
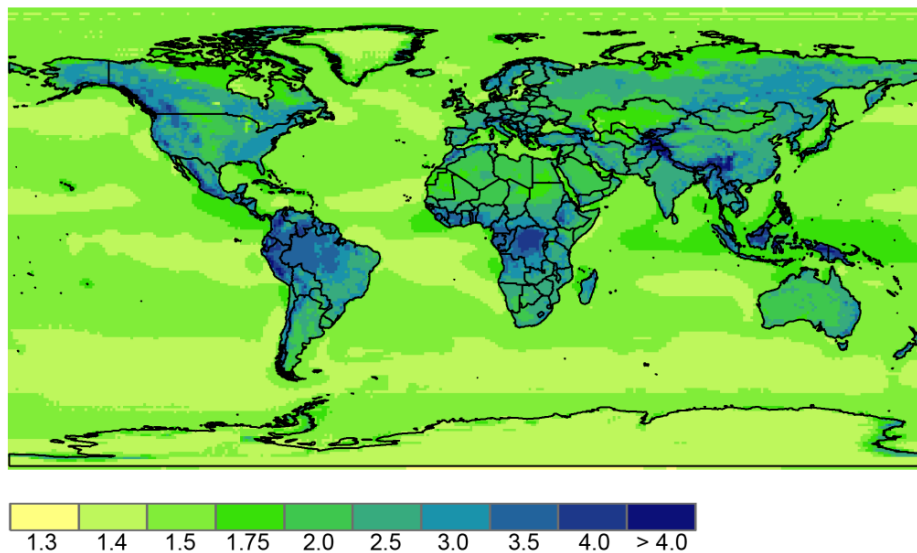
Figure 3. Median gust factor ($\widetilde{GF}$) in the investigation period.

3.3. Monthly Gust Characteristics

In many regions around the world, *GS* characteristics vary within a year. Therefore, annual cycles of GS_{50yr}, *SOC* and $\widetilde{GF}$ are presented for six grid cells in Figure 4. These grid cells represent regions of the six countries with the highest CO_2 emissions in 2015 [47], where high $\overline{WPD}$ values offer a good meteorological wind energy potential and are not restricted due to geographical constraints. Highest GS_{50yr} values for a grid cell related to China (24.02° N, 117.61° E) occur in July and October (29 m s^{-1}) (Figure 4a). *SOC* values throughout the year are low. Only in July and October *GS* values above 25.0 m s^{-1} occur. It is remarkable that highest $\overline{WPD}$ values (>600 W m^{-2}) were simulated in November and December, when GS_{50yr} does not exceed 24.0 m s^{-1} and *SOC* = 0.0%. This example demonstrates that highest $\overline{WPD}$ and *GS* can occur independently of each other. In contrast to GS_{50yr}, *SOC* and $\overline{WPD}$, $\widetilde{GF}$ is nearly constant throughout the year. In June, July, and August $\widetilde{GF}$ is 1.6, whereas in all other months $\widetilde{GF}$ = 1.5.

Highest GS_{50yr} values related to a grid cell in the USA (35.91° N, 100.18° W) occur in April (Figure 4b). In the same month, *SOC* (0.3%) and $\overline{WPD}$ (343 W m^{-2}) exceed the values related to all other months. Lowest GS_{50yr} (19 m s^{-1}) and $\overline{WPD}$ (158 W m^{-2}) was simulated in August. The $\widetilde{GF}$ values (1.7–1.8) are slightly higher than at the grid point related to China, indicating a more pronounced gustiness of the airflow. The $\widetilde{GF}$ variations throughout the year are small. This emphasizes that $\widetilde{GF}$ is rather driven by surface characteristics than by large-scale air flow variations throughout the year.

Due to the Indian monsoon, the $\overline{WPD}$ regime of a grid cell related to India (8.32° N, 77.72° E) is characterized by two maxima (Figure 4c). The highest $\overline{WPD}$ values of the first maximum occurring in summer were simulated in June (806 W m^{-2}). In winter, when the second maximum happens, $\overline{WPD}$ reaches values up to 488 W m^{-2}. The GS_{50yr} values are comparatively low (<20 m s^{-1}). The $\widetilde{GF}$

values lie in the range of 1.4–1.6. GS values exceeding 25.0 m s^{-1} were not simulated in the investigation period, therefore SOC = 0.0% in all months.

In Japan (40.70° N, 141.12° E), $\overline{WPD}$ values in winter are clearly higher (>800 W m^{-2}) than in summer ($\overline{WPD}$ > 150 W m^{-2}) (Figure 4d). The highest GS_{50yr} values occur in February (40 m s^{-1}). In September, GS_{50yr} = 34 m s^{-1}, although $\overline{WPD}$ is rather low (205 W m^{-2}). This is due to the influence of typhoons, which only last for a short period, so that their influence on $\overline{WPD}$ is small. From August to April, *GS* exceeds 25 m s^{-1} several times (0.1–0.7%). In contrast to results presented for China, the USA and India the $\widetilde{GF}$ values in summer (~1.4) are lower than in winter (~1.6). Thus, it must be noted that the great wind energy potential in winter is accompanied by gusts.

In Russia (61.30° N, 32.26° E), the highest $\overline{WPD}$ values were simulated in November (408 W m^{-2}) (Figure 4e). The GS_{50yr} maximum (25.0 m s^{-1}) is simulated in the same months. Lowest $\overline{WPD}$ (100 W m^{-2}) and GS_{50yr} (19 m s^{-1}) occur in July. Cut-out wind speed is not exceeded (*SOC* = 0.0%). Thus, losses due to shut-downs of wind turbines during storm events are no serious issue in this region. The $\widetilde{GF}$ values lie between 1.4–1.5 throughout the year, indicating an overall low turbulence.

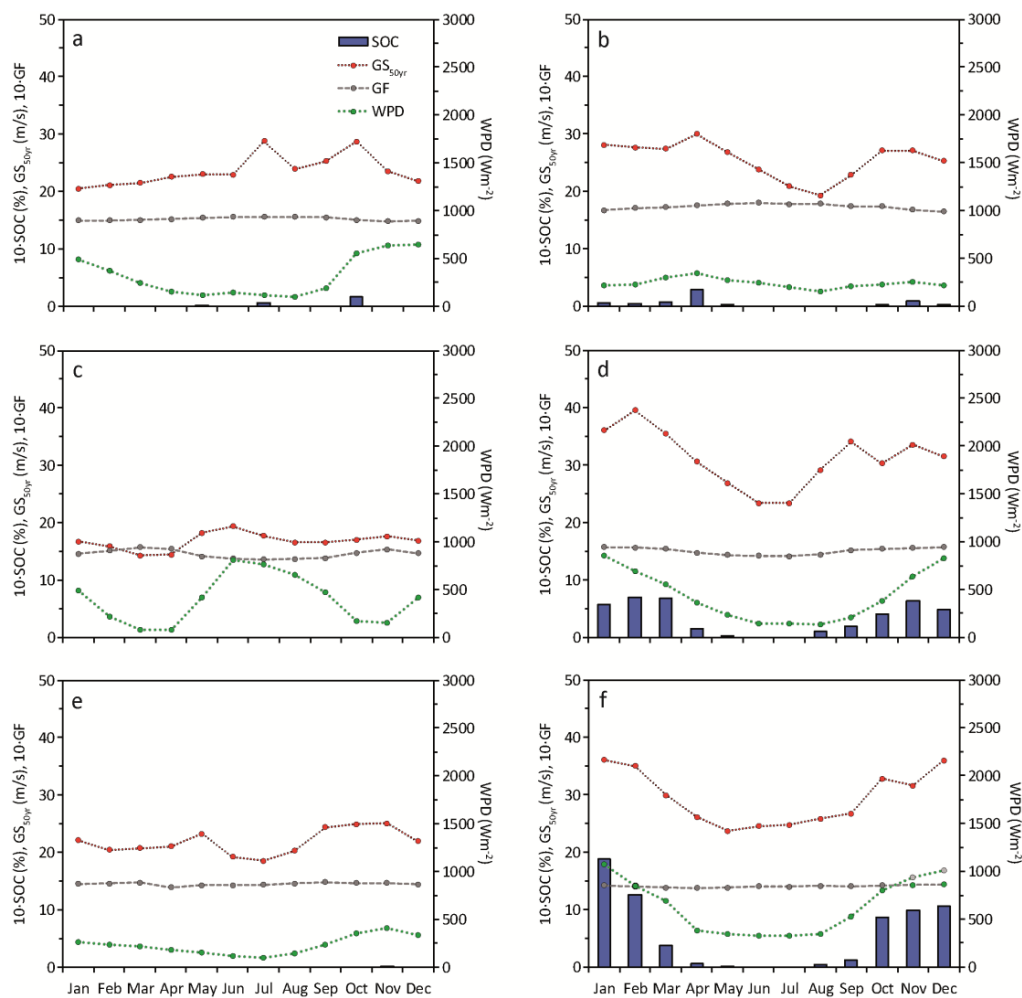**Figure 4.** Annual cycle of monthly gust speed (*GS*) values for a return period of 50 years (GS_{50yr}), share of three-hour periods when gust speed *GS* exceeds 25.0 m s^{-1} (*SOC*), median gust factor ($\widetilde{GF}$), and mean wind power density ($\overline{WPD}$). Each variable is presented for grid points related to the six countries with highest CO$_2$ emissions in 2015: (**a**) China; (**b**) USA; (**c**) India; (**d**) Russia; (**e**) Japan; and (**f**) Germany.

The yearly $\overline{WPD}$ cycle for a grid cell related to Northwestern Germany (53.58° N, 7.29° E) is characterized by a maximum in January (1070 W m^{-2}) and a minimum in July (326 W m^{-2}) (Figure 4f). The high $\overline{WPD}$ values are accompanied by extreme GS_{50yr} values (December and January: 36 m s^{-1}). In contrast to all other examples presented so far, *SOC* values exceed 1.0% from November to February. Northwestern Germany is regularly influenced by windstorms in winter. Although these events ensure great wind energy potential, the windstorm-related gusts must be recognized as being potentially destructive and causing periods where no wind energy can be generated. The $\widetilde{GF}$ values are low throughout the whole year (1.4).

In Figure 5, annual cycles of GS_{50yr}, *SOC* and $\widetilde{GF}$ are presented for six regions, which offer a good to great wind energy potential (>700 W m^{-2} in one month). The extreme wind climate related to a grid point near the Canadian east coast (53.60° N, 56.34° W) is characterized by very high GS_{50yr} values that exceed 30 m s^{-1} in all months, except June, July and August (Figure 5a). The highest GS_{50yr} values were simulated in March (41 m s^{-1}). From November to February, $(\overline{WPD} > 1000$ W m$^{-2})$. However, periods where *GS* exceeds cut-out speed are frequent, with the highest *SOC* values occurring from December to February (4.7%, 5.2%, and 3.8%). Only in June, July, and August *SOC* = 0.0%. The $\widetilde{GF}$ values are 1.4 throughout the whole year.

The annual $\overline{WPD}$ variation in Argentina (51.86° S, 69.12° W) is relatively small. The $\overline{WPD}$ values lie between 610 W m^{-2} in May and 895 W m^{-2} in November (Figure 5b). Except for July, GS_{50yr} is at least 30 m s^{-1} in all months, but does not exceed 35 m s^{-1}. Periods where *GS* > 25.0 m s^{-1} occur on a regular base, ranging from 0.4% in July to 1.4 in November and February. Thus, losses due to high *GS* values must be considered. The gustiness of the airflow is small, therefore $\widetilde{GF}$ lies between 1.4 in November and December and 1.5 in all other months.
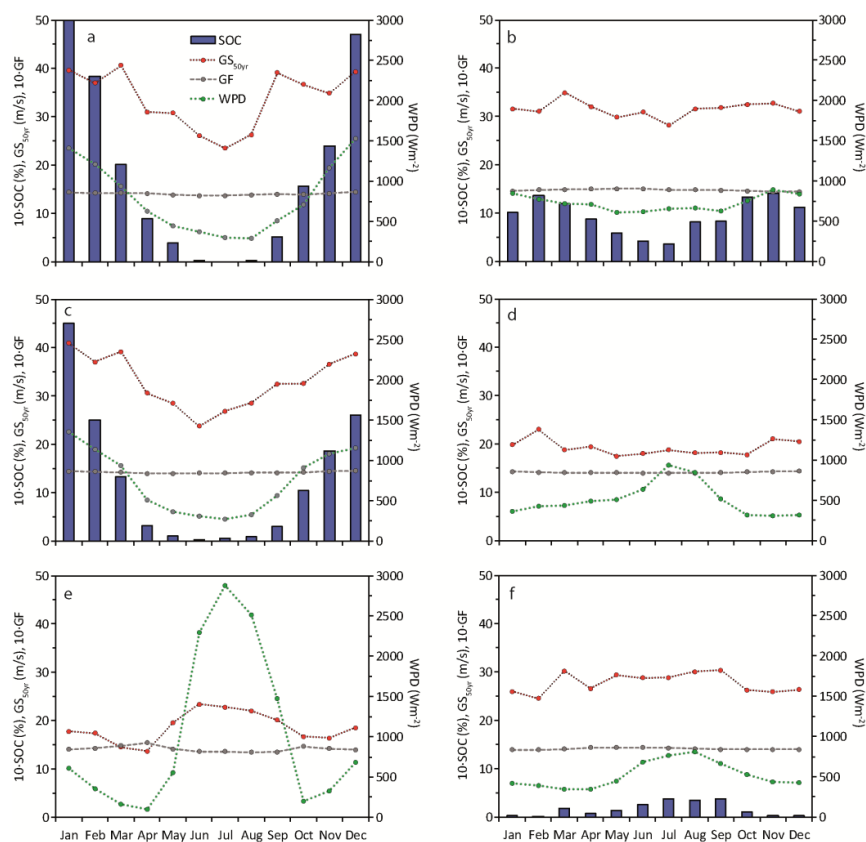

Figure 5. Annual cycle of monthly gust speed (*GS*) values for a return period of 50 years (GS_{50yr}), share of three-hour periods when *GS* exceeds 25.0 m s^{-1}, median gust factor ($\widetilde{GF}$), and mean wind power density ($\overline{WPD}$). Each variable is presented for grid points related to (**a**) Canada; (**b**) Argentina; (**c**) Great Britain; (**d**) Western Sahara; (**e**) Somalia; and (**f**) Australia.

The annual *GS* characteristics for a grid point related to Great Britain (57.61° N, 2.07° W) are similar to those presented for Canada (Figure 5c). The percentage share of $GS > 25.0$ m s^{-1} exceeds 1.0% between November and March. In January GS_{50yr} reaches 41 m s^{-1}. The lowest GS_{50yr} was simulated in June (24 m s^{-1}). The $\overline{WPD}$ values related to the grid cell are higher than 900 W m^{-2} between October and March. From May to August, the wind energy potential is smaller ($\overline{WPD} < 400$ W m^{-2}). The variable that has the lowest variability throughout the year is $\widetilde{GF}$. Except for December (1.5), it is 1.4 in all months.

The *GS* properties related to a grid point of the Western Sahara (25.64° N, 14.55° W) greatly differ from the previously presented results (Figure 5d). In the Western Sahara, northeasterly trade winds dominate, whereas the wind climate in Canada, Argentina, and Great Britain is mainly influenced by the west wind drift. GS_{50yr} does not exceed 25 m s^{-1}, consequently *SOC* is 0 in all months. From March to October GS_{50yr} is below 20 m s^{-1}. The highest GS_{50yr} value (23 m s^{-1}) occurs in February. The surface roughness in the Western Sahara is low, thus $\widetilde{GF}$ is only 1.4 in all months. The maximum of the trade winds occurs in July, therefore ($\overline{WPD} = 941$ W m^{-2}). The lowest $\overline{WPD}$ value was simulated in November (310 W m^{-2}).

The Indian summer monsoon is a special case of trade winds, which induces southwesterly airflow at the Horn of Africa. Thus, in Somalia (9.37° N, 50.60° E) $\overline{WPD}$ values in June (2294 W m^{-2}), July (2873 W m^{-2}) and August (2516 W m^{-2}) are exceptionally high (Figure 5e). Nevertheless, GS_{50yr} does not exceed 25 m s^{-1} in these months. These values indicate that air flow is constant, but not gusty. Consequently, $\widetilde{GF}$ values are very low, especially in August (1.3). Such conditions are very favorable for wind energy utilization. The northeasterly winter monsoon leads to a secondary $\overline{WPD}$ maximum from November to February, where $\overline{WPD}$ values are between 329 W m^{-2} and 683 W m^{-2}. The corresponding GS_{50yr} values are below 20 m s^{-1}. In April lowest $\overline{WPD}$ values are simulated (96 W m^{-2}).

In Australia (37.71° S, 140.42° E), the highest GS_{50yr} values (30 m s^{-1}) occur in August and September (Figure 5f). The monthly GS_{50yr} variability is small, since the lowest GS_{50yr} value in February is 25 m s^{-1}. The *SOC* values between March and October are in the range between 0.1% and 0.4%. In all other months GS_{50yr} values do not exceed 25.0 m s^{-1}. Similar to the annual GS_{50yr} cycle the maximum $\overline{WPD}$ values were simulated in August (813 W m^{-2}). The $\widetilde{GF}$ values are low throughout the whole year (1.4).

The results that were presented in the previous section showed that the latitude has a great influence on *GC*. In order to highlight its impact, GS_{50yr}, *SOC*, and $\widetilde{GF}$ were averaged over all longitudes separately for all months. For better comparability $\overline{WPD}$ was also averaged over all longitudes and is presented in Figure 6a. It reveals that meteorological wind energy potential is highest between 40° S and 70° S, where $\overline{WPD}$ peaks at 54° S in August (1834 W m^{-2}). $\overline{WPD}$ values in this area are highest in all months, but most clearly exceed $\overline{WPD}$ values of all other latitudes from June to August. The corresponding latitudes of the northern hemisphere are characterized by clearly lower $\overline{WPD}$ values and a pronounced annual cycle. This is due to the rough surfaces of the continents, whereas the southern hemisphere is predominantly covered by oceans. The lowest $\overline{WPD}$ can be found at the equator in April (64 W m^{-2}). Local $\overline{WPD}$ maxima occur between 10° N and 20° N in the winter months and 10° S and 20° S in the summer months.

The distribution of GS_{50yr} values shows some differences from $\overline{WPD}$ (Figure 6b). With increasing proximity to the equator, GS_{50yr} values decrease virtually linear to 12 m s^{-1} in April. This is due to the fact that trade winds are constant rather than gusty. The maximum GS_{50yr} value occurs at 67° S in July and August. This is near the Antarctic shore, where the transition zone between water and ice induces high *GS* values. The mid-latitudes of the northern hemisphere show a profound annual cycle with minimum GS_{50yr} values in July and maximum GS_{50yr} values in December and January.

The monthly *SOC* values are presented in Figure 6c. Virtually no *GS* values exceed 25.0 m s^{-1} between 30° N and 30° S. The maximum *SOC* value in January is at 58° N (2.49%), whereas the maximum *SOC* value in August is at 55° S (4.74%). These results indicate that the extratropical

cyclones are the main reasons for *GS* values exceeding cut-out speed, and thus induce periods where no wind energy can be produced.

Since $\widetilde{GF}$ is mainly influenced by surface roughness, their variability is determined by the distributions of land and ocean surfaces (Figure 6d). Highest $\widetilde{GF}$ values (2.2) were simulated at 61° N in June. At this latitude, the land surfaces of Russia and Canada cover large parts of the earth surface. The monthly variability of $\widetilde{GF}$ is due to the fact that $\widetilde{GF}$ increases with decreasing *x*, which occur at the mid-latitudes in summer months. The minimum $\widetilde{GF}$ value occurs at 82° S from March to October (1.3). This is due to the low surface roughness of the Antarctic ice sheet.
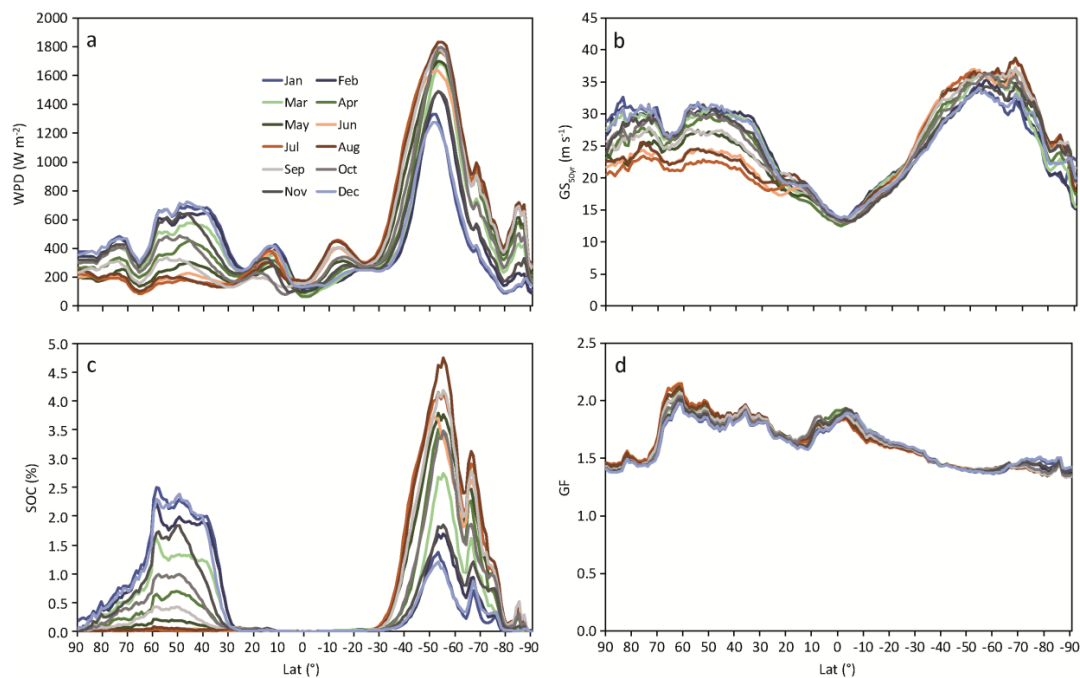
Figure 6. Monthly (**a**) mean wind power density ($\overline{WPD}$); (**b**) gust speed (*GS*) values for a return period of 50 years (GS_{50yr}); (**c**) share of three-hour periods when *GS* exceeds 25.0 m s^{-1} (*SOC*); and (**d**) median gust factor ($\widetilde{GF}$) in the investigation period as a function of latitude (*Lat*). These variables were averaged over all longitudes.

3.4. Wind Turbine Gust Index

The variables GS_{50yr}, *SOC* and $\widetilde{GF}$ were integrated into *WTGI* to yield a relative assessment of the influence of gusts on wind turbines and power generation. The global distribution of onshore *WTGI* is presented for all non-geographically restricted areas without considering $\overline{WPD}$ (Figure 7a) and where $\overline{WPD} > 50$ W m^{-2} (Figure 7b). The largest continuous areas that are most seriously negatively affected by gusts (*WTGI* = 8) and where $\overline{WPD}$ exceeds 50 W m^{-2} can be found in the Northeastern United States, in Southeast Canada, Newfoundland, the southern tip of South America, and Northwestern Europe. The west coast of North America, Iceland, South Africa, northern parts of Madagascar, west coast of Scandinavia, Tasmania, New Zealand, South Korea, Japan, the Midwestern United States, and parts of Northeast China are also characterized by high *WTGI* values. Lowest *WTGI* values in areas, where $\overline{WPD} > 50$ W m^{-2}, mainly occur in eastern Brazil, in the Sahara, southern parts of Somalia, and southeastern parts of the Arabian Peninsula. These results indicate that areas where trade winds dominate are less influenced by negative gust effects than areas in the mid-latitudes.
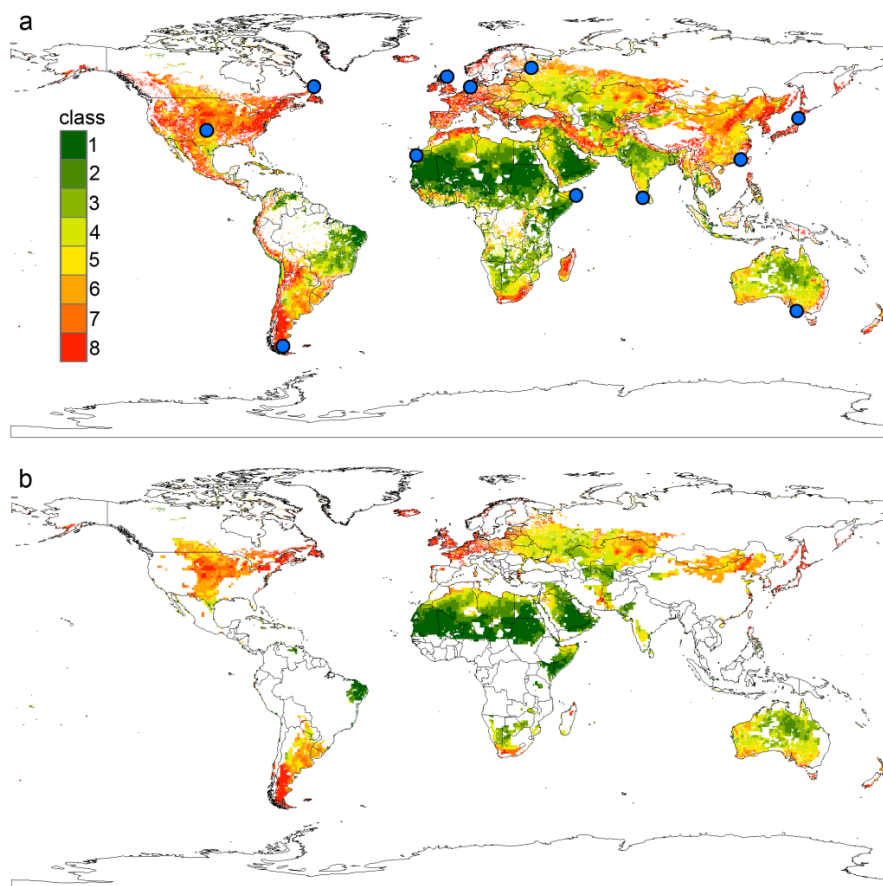
Figure 7. Global distribution of the onshore wind turbine gust index (*WTGI*) (**a**) for all non-geographically restricted areas and (**b**) for all non-geographically restricted areas where mean wind power density exceeds 50 W m^{-2}.

$\overline{WPD}$ exceeds 50 W m^{-2} in almost all offshore areas (Figure 8). Highest *WTGI* offshore values can be found near Alaska and Iceland. In the North Sea region, the Sea of Okhotsk, and the Canadian east coast, high *WTGI* values indicate a strong influence of *GS*. Lowest *WTGI* values occur along the northwestern coast of South America, the Red Sea, the Persian Gulf, Southeast Asia, and the Arafura Sea.
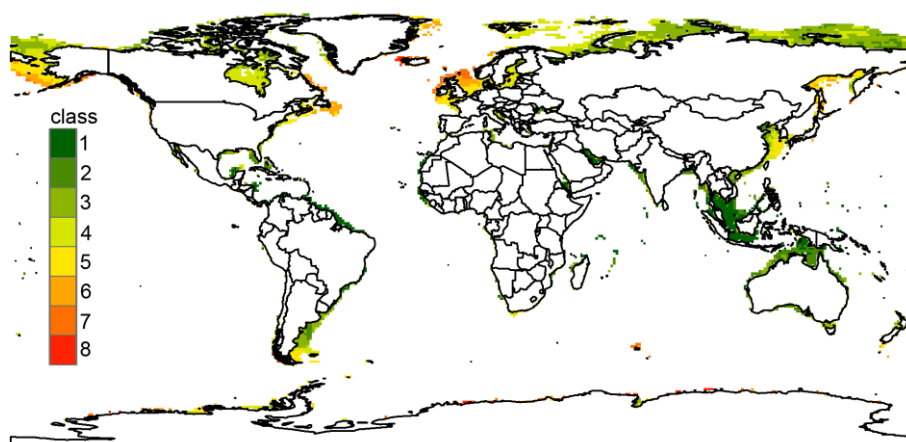

Figure 8. Global distribution of the offshore wind turbine gust index (*WTGI*), where sea depth <200 m.

4. Conclusions

The influence of gust characteristics on wind energy production was assessed at the global scale. It was found that in the mid-latitudes, where the west wind drift dominates, wind turbines are exposed to gust speeds that frequently exceed cut-out speed and lead to shut-downs of wind turbines. In regions where the trade winds dominate, the frequency of gust speeds that disturb wind energy production is much lower. In areas with rough surfaces (e.g., forests or large mountain ranges) the high level of gustiness may also negatively influence the technical integrity of wind turbines. The effects of gusts on wind turbine operations were classified by integrating gust characteristics into the wind turbine gust index *WTGI*.

The presented assessment of the influence of gust characteristics on wind energy production will be helpful for future large-scale and globally coordinated planning of wind turbine installation. In areas where surface properties influence gust characteristics at the local scale, it is suggested to develop the methodology further to a high spatial resolution assessment. From a previous study an approach exists that allows for mapping gust speed distributions on a high spatial resolution (50 m × 50 m) scale in small study areas [13]. In that study, Wakeby parameters were modeled by an LSBoost approach using sector and distance-limited predictors of surface roughness and terrain-related variables (curvature, elevation, topographic exposure) as well as on ERA-Interim reanalysis wind speed data available at the 850 hPa pressure level. Combining the methodologies of both studies enables the development of gust characteristic maps on a high spatial resolution scale in small study areas. One important requirement to adopt the methodology to small study areas is that long-term gust speed time series exist.

Author Contributions: Christopher Jung conceived and designed the study; Alexander Buchholz, Christopher Jung and Jessica Laible analyzed the data; Dirk Schindler provided guidance; Christopher Jung wrote the paper; Dirk Schindler co-wrote the paper.

Conflicts of Interest: The authors declare no conflict of interest.

Nomenclature

Acronyms

cdf	cumulative distribution function
ecdf	empirical cumulative distribution function
epdf	empirical probability density function
G	two-parameter Gamma distribution
GEV	three-parameter Generalized Extreme Value distribution
GL	three-parameter Generalized Logistic distribution
GN	three-parameter Generalized Normal distribution
GoF	goodness-of-fit
GP	three-parameter Generalized Pareto distribution
Gu	two-parameter Gumbel distribution
K	four-parameter Kappa distribution
L	two-parameter Lognormal distribution
L3	three-parameter Lognormal distribution
LM	L-moment method
M	Moment method
ML	Maximum Likelihood estimation
P3	three-parameter Pearson 3 distribution
PEM	parameter estimation method
S	abbreviation
Wak	five-parameter Wakeby distribution
Wei	two-parameter Weibull distribution

Symbols

$\hat{F}$	estimated cumulative distribution function
$\widetilde{GF}$	median gust factor
$\overline{WPD}$	mean wind power density
AD	Anderson–Darling statistic
APR	atmospheric pressure
F	cumulative distribution function
F^{-1}	quantile function
GC	gust characteristic
GC'	normalized gust characteristic
GF	gust factor
GS	gust speed
KS	Kolmogorov–Smirnov statistic
Lat	latitude
Lon	longitude
n	sample size
NP	number of parameters
R	atmospheric gas constant
RP	return period
SOC	percentage number of exceedances of cut-out speed
TA	air temperature
T	return period
u	zonal wind vector component
v	meridional wind vector component
WPD	wind power density
$WTGI$	wind turbine gust index
x	wind speed
α	first scale parameter
β	first shape parameter
γ	second scale parameter
δ	second shape parameter
ε	location parameters
ρ	air density

Subscripts

$100yr$	100-year return period
$30yr$	30-year return period
$50yr$	50-year return period
max	maximum
min	minimum
i	ith value of data sample
WAK	Wakeby distribution

References

1. Payne, J.E. A survey of the electricity consumption-growth literature. *Appl. Energy* **2010**, *87*, 723–731. [CrossRef]
2. Panteli, M.; Mancarella, P. Influence of extreme weather and climate change on the resilience of power systems: Impacts and possible mitigation strategies. *Electr. Power Syst. Res.* **2015**, *127*, 259–270. [CrossRef]
3. Campbell, R.J. *Weather-Related Power Outages and Electric System Resiliency*; Congressional Research Service: Washington, DC, USA, 2012.
4. Cadini, F.; Agliardi, G.L.; Zio, E. A modeling and simulation framework for the reliability/availability assessment of a power transmission grid subject to cascading failures under extreme weather conditions. *Appl. Energy* **2017**, *185*, 267–279. [CrossRef]

5. He, W.; Ge, S.S. Vibration control of a nonuniform wind turbine tower via disturbance observer. *IEEE ASME Trans. Mechatron.* **2015**, *20*, 237–244. [CrossRef]

6. Durst, C.S. Wind speeds over short periods of time. *Meteorol. Mag.* **1960**, *89*, 181–186.

7. Jung, C.; Schindler, D.; Albrecht, A.; Buchholz, A. The role of highly-resolved gust speed in simulations of storm damage in forests at the landscape scale: A case study from southwest Germany. *Atmosphere* **2016**, *7*, 7. [CrossRef]

8. Wang, J.; Qin, S.; Jin, S.; Wu, J. Estimation methods review and analysis of offshore extreme wind speeds and wind energy resources. *Renew. Sustain. Energy Rev.* **2015**, *42*, 26–42. [CrossRef]

9. Quaschning, V. *Regenerative Energiesysteme. Technologie—Berechnung—Simulation*, 9th ed.; Carl Hanser Verlag GmbH & Co.: München, Germany, 2011; ISBN 978-3-446-44267-2.

10. Morgan, E.C.; Lackner, M.; Vogel, R.M.; Baise, L.G. Probability distributions for offshore wind speeds. *Energy Convers. Manag.* **2011**, *52*, 15–26. [CrossRef]

11. Lydia, M.; Kumar, S.S.; Selvakumar, A.I.; Prem Kumar, G.E. A comprehensive review on wind turbine power curve modeling techniques. *Renew. Sustain. Energy Rev.* **2014**, *30*, 452–460. [CrossRef]

12. Manwell, J.F.; McGowan, J.G.; Rogers, A.L. *Wind Energy Explained: Theory, Design and Application*, 2nd ed.; John Wiley & Sons: Chichester, UK, 2009; ISBN 978-0470015001.

13. Jung, C.; Schindler, D. Modelling monthly near-surface maximum daily gust speed distributions in Southwest Germany. *Int. J. Climatol.* **2016**, *36*, 4058–4070. [CrossRef]

14. Haanpää, S.; Lehtonen, S.; Peltonen, L.; Talockaite, E. Impacts of Winter Storm Gudrun of 7th–9th January 2005 and Measures Taken in Baltic Sea Region. Available online: http://www.astra-project.org/06_winterstorm_study.html (accessed on 27 August 2017).

15. Lee, B.-H.; Ahn, D.-J.; Kim, H.-G.; Ha, Y.-C. An estimation of the extreme wind speed using the Korea wind map. *Renew. Energy* **2012**, *42*, 4–10. [CrossRef]

16. Chang, P.-C.; Yang, R.-Y.; Lai, C.-M. Potential of Offshore Wind Energy and Extreme Wind Speed Forecasting on the West Coast of Taiwan. *Energies* **2015**, *8*, 1685–1700. [CrossRef]

17. Kang, D.; Ko, K.; Huh, J. Determination of extreme wind values using the Gumbel distribution. *Energy* **2015**, *86*, 51–58. [CrossRef]

18. Pes, M.P.; Pereira, E.B.; Marengo, J.A.; Martins, F.R.; Heinemann, D.; Schmidt, M. Climate trends on the extreme winds in Brazil. *Renew. Energy* **2017**, *109*, 110–120. [CrossRef]

19. Gong, K.; Ding, J.; Chen, X. Estimation of long-term extreme response of operational and parked wind turbines: Validation and some new insights. *Eng. Struct.* **2014**, *81*, 135–147. [CrossRef]

20. Chiodo, E.; De Falco, P. Inverse Burr distribution for extreme wind speed prediction: Genesis, identification and estimation. *Electr. Power Syst. Res.* **2016**, *141*, 549–561. [CrossRef]

21. Dee, D.P.; Uppala, S.M.; Simmons, A.J.; Berrisford, P.; Poli, P.; Kobayashi, S.; Andrae, U.; Balmaseda, M.A.; Balsamo, G.; Bauer, P.; et al. The ERA-Interim reanalysis: Configuration and performance of the data assimilation system. *Q. J. R. Meteorol. Soc.* **2011**, *137*, 553–597. [CrossRef]

22. WMO Guide to Meteorological Instruments and Methods of Observations. Available online: https://library.wmo.int/opac/doc_num.php?explnum_id=3177 (accessed on 27 August 2017).

23. Hellman, G. Über die Bewegung der Luft in den untersten Schichten der Atmosphäre. *Meteorol. Z.* **1915**, *32*, 1–16. (In German)

24. Deacon, E.L. Gust variation with height up to 150 m. *Q. J. R. Meteorol. Soc.* **1955**, *81*, 562–573. [CrossRef]

25. Grau, L.; Jung, C.; Schindler, D. On the annual cycle of meteorological and geographical potential of wind energy: A case study from Southwest Germany. *Sustainability* **2017**, *9*, 1169.

26. Kim, J.-Y.; Kim, H.-G.; Kang, Y.-H. Offshore wind speed forecasting: The correlation between satellite-observed monthly sea surface temperature and wind speed over the seas around the Korean peninsula. *Energies* **2017**, *10*, 994.

27. Cehak, K. Der Jahresgang der monatlichen höchsten Windgeschwindigkeiten in der Darstellung durch Fisher-Tippett III-Verteilungen. *Arch. Meteorol. Geophys. Bioklimatol.* **1971**, *19*, 165–182. (In German) [CrossRef]

28. Friederichs, P.; Göber, M.; Bentzien, S.; Lenz, A.; Krampitz, R. A probabilistic analysis of wind gusts using extreme value statistics. *Meteorol. Z.* **2009**, *18*, 615–629. [CrossRef] [PubMed]

29. Jung, C.; Schindler, D. Global comparison of the goodness-of-fit of wind speed distributions. *Energy Convers. Manag.* **2017**, *133*, 216–234. [CrossRef]

30. Massey, F.J. The Kolmogorov-Smirnov test for goodness of fit. *J. Am. Stat. Assoc.* **1951**, *46*, 68–78. [CrossRef]

31. Anderson, T.W.; Darling, D.A. A test of goodness of fit. *J. Am. Stat. Assoc.* **1954**, *49*, 765–769. [CrossRef]

32. Jung, C.; Schindler, D.; Laible, J.; Buchholz, A. Introducing a system of wind speed distributions for modeling properties of wind speed regimes around the world. *Energy Convers. Manag.* **2017**, *144*, 181–192. [CrossRef]

33. Houghton, J.C. Birth of a parent: The Wakeby distribution for modeling flood flows. *Water Resour. Res.* **1978**, *14*, 1105–1109. [CrossRef]

34. Jung, C. High spatial resolution simulation of annual wind energy yield using near-surface wind speed time series. *Energies* **2016**, *9*, 344. [CrossRef]

35. Rahman, A.; Zaman, M.A.; Haddad, K.; El Adlouni, S.; Zhang, C. Applicability of Wakeby distribution in flood frequency analysis: a case study for eastern Australia. *Hydrol. Process.* **2015**, *29*, 602–614. [CrossRef]

36. Hosking, J.; Wallis, J. *Regional Frequency Analysis: An Approach Based on L-Moments*; Cambridge University Press: Cambridge, UK, 1997.

37. Schindler, D.; Jung, C.; Buchholz, A. Using highly resolved maximum gust speed as predictor for forest storm damage caused by the high-impact winter storm Lothar in Southwest Germany. *Atmos. Sci. Lett.* **2016**, *17*, 462–469. [CrossRef]

38. Jung, C.; Schindler, D. Development of a statistical bivariate wind speed-wind shear model (WSWS) to quantify the height-dependent wind resource. *Energy Convers. Manag.* **2017**, *149*, 303–317. [CrossRef]

39. Loveland, T.R.; Reed, B.C.; Brown, J.F.; Ohlen, D.O.; Zhu, Z.; Yang, L.; Merchant, J.W. Development of a global land cover characteristics database and IGBP DISCover from 1 km AVHRR data. *Int. J. Remote Sens.* **2000**, *21*, 1303–1330. [CrossRef]

40. The World Database on Protected Areas (WDPA). Available online: https://www.iucn.org/theme/protected-areas/our-work/world-database-protected-areas (accessed on 3 August 2017).

41. Danielson, J.J.; Gesch, D.B. *Global Multi-Resolution Terrain Elevation Data 2010 (GMTED2010)*; Open-File Report 2011-1073; U.S. Geological Survey: Reston, VA, USA, 2011.

42. Mentis, D.; Hermann, S.; Howells, M.; Welsch, M.; Siyal, S.H. Assessing the technical wind energy potential in Africa a GIS-based approach. *Renew. Energy* **2015**, *83*, 110–125. [CrossRef]

43. Gruber, S. Derivation and analysis of a high-resolution estimate of global permafrost zonation. *Cryosphere* **2012**, *6*, 221–233. [CrossRef]

44. Global Permafrost Zonation Index Map. Available online: http://www.geo.uzh.ch/microsite/cryodata/pf_global/ (accessed on 3 August 2017).

45. Lu, X.; McElroy, M.B.; Kiviluoma, J. Global potential for wind-generated electricity. *Proc. Natl. Acad. Sci. USA* **2009**, *106*, 10933–10938. [CrossRef] [PubMed]

46. Wieringa, J. Roughness-dependent geographical interpolation of surface wind speed averages. *Q. J. R. Met. Soc.* **1986**, *112*, 867–889. [CrossRef]

47. Global Carbon Atlas. Available online: http://www.globalcarbonatlas.org/en/CO2-emissions (accessed on 3 August 2017).